Chapter 2

Statistical Study of Limb Flares Observed by *RHESSI* : Imaging and Imaging Spectroscopy

2.1 Introduction

Observations of solar flares by low spectral and spatial resolution instruments can give us only the light curve and a crude spectrum of the whole flare which may consist of many distinct sources with different characteristics. The discovery of distinct looptop (LT) sources (Sakao, 1994; Masuda, 1994) in addition to the normal footpoint (FP) sources, made by the *Yohkoh* satellite, has provided further evidence for the stochastic acceleration model (Petrosian & Donaghy, 1999; Petrosian et al., 2002) which was shown to be consistent with the broadband spectra of several solar flares (Park et al. 1997). As suggested by this and other models, these different sources should have different electron spectra determined by the physical condition at the acceleration site. Statistical studies of FP-to-LT flux ratios have been conducted for *Yohkoh* flares (Petrosian et al., 2002; Tomczak & Ciborski, 2007).

The exceptional imaging spectroscopic capacity of *RHESSI* (Lin et al. 2002), combined with its excellent time resolution, provides us a multi-dimensional picture of solar flares, which can set stringent constraints on the model parameters and will eventually improve our understanding of the relevant physical processes.

One important aspect of such constraints can be obtained from the spectral correlation of the FP and LT sources. In the stochastic acceleration model the LT emission comes directly from the accelerated electrons (thin target) while the FP emission is produced by the escaping electrons in a thick target region. The flux and spectra of the two sources are related. The exact relation depends on various acceleration mechanism and plasma parameters but very roughly the FP to LT X-ray flux ratio at photon energy E can be written as (see Petrosian & Donaghy 1999 and eq. [7.23]) $I_{FP}/I_{LT} \simeq \tau_{\mathrm{loss}}(E)/T_{\mathrm{esc}}(E)$, where $\tau_{\mathrm{loss}} = E/\dot{E}_L$ is the electron energy loss time at the LT (due to Coulomb collision at low energies and synchrotron loss at high energies), and the energy dependence of the escape time T_{esc} (see, e.g., eq. [7.20]) depends on the details of the acceleration process in the LT region. This means that the relative spectra can constrain the plasma and acceleration

model parameters. At low energies, for example, $\tau_{\mathrm{loss}} \propto E^{3/2}$ (since $\dot{E}_{\mathrm{Coul}} \propto 1/\beta$, see eq. [7.3]), and thus the functional form of $T_{\mathrm{esc}}(E)$ can be directly obtained from the observed flux ratio.

A statistical study of the relative spectra of different sources is thus required to obtain such observational constraints with sufficient statistical confidence. We carefully selected a sample of 29 limb flares, which may provide some statistical information on LT and FP emissions. Battaglia & Benz (2006) recently reported a similar study of five *RHESSI* flares. A larger sample of events has not been practically feasible in the past, given the evolving *RHESSI* instrument calibration and software on the early stage of the mission (launched 2002), but we look forward to expanding our sample in the future.

We present in this chapter images, light curves of the LT and FP sources of the sample flares, as well as their imaging spectroscopy. We describe the flare selection criteria and the imaging procedure in §2.2. Results from case studies of typical events are given in §2.3. Statistics of various parameters is presented in §2.4 and §2.5. Finally we conclude this chapter with §2.6. Discussions on miscellaneous data analysis techniques used in this study are given in Appendices §A.1 and §A.2.

2.2 Data Reduction and Analysis

2.2.1 Sample Selection Criteria

We searched through the online *RHESSI* flare list (from February 12, 2002 through April 18, 2004[1]) for appropriate limb flares, using criteria similar to those introduced by Masuda (1994) and used by Petrosian et al. (2002), which are:

- Heliocentric longitude ≥ 70 degrees. This provides sufficient angular separation between FP and LT sources. The heliocentric (x, y) coordinates in the *RHESSI* flare list[2] were converted to heliographic (longitude, latitude) coordinates[3]. For flares whose locations are not available in the list, we obtained the locations by making full disk *RHESSI* images, usually in the 12–25 keV energy channel about the peak time, and used the position of the brightest pixel as the flare location.

- Peak count rate ≥ 30 per second per detector in the 12–25 keV channel, allowing sufficient count statistics and thus good image quality.

We then carefully examined the sample flares satisfying these criteria and eliminated those with strong particle events, severe pileup or decimation, or poor data quality. There are 29 flares included in our final sample, which are listed in Table 2.1. The heliographic locations (*left*) and the distribution of the peak count rate (*right*) at 12–25 keV are shown Figure 2.1. For each sample event, we performed imaging spectroscopy and light curve study as follows.

---

[1] The analysis presented here was initiated back in 2003 using the *RHESSI* software existing then. New flares were added to the latest sample as of April 18, 2004. The software has been improved since then and thus may give slightly different results.

[2] see http://hesperia.gsfc.nasa.gov/hessidata/dbase/hessi_flare_list.txt

[3] We used xy2lonlat.pro in the *Solar SoftWare* package to do the conversion. For flare locations off the limb, the corresponding positions projected back to the limb were used. These flares may have a longitude greater than $90°$ (see Table 2.1), because the solar pole is not aligned in the plane of the sky.

Table 2.1: List of $(22 + 7 = 29)$ flare events included in this study.

Flare ID (ymmdd#)	Peak time (UT)	Disk position	NOAA AR #	GOES class	Peak Count	Highest E-band (keV)	Image spec. (Y/N)	Notes
2022003	11:06:18	N13W73?	-	C7.5	656	50-100		3 FPs, no LT?
2032819	17:58:18	S04W90	-	C7.6	200	25-50		one source (LT)?
2041509	23:12:26	N21W77	9893?	M1.2	816	25-50		complex^T
2051706	07:38:10	N13E89?	-	M1.5	1328	25-50		2 LTs?
2051909	21:46:22	S23E78	-	C4.7	84	25-50		source not well def.
2062904	09:29:46	S17E79	-	C2.0	352	12-25		single loop
2072301	00:30:06	S13E74	0039	X4.8	57379	800-7000	Y	complex^T
2072307	12:21:42	S19E78	-	C2.9	240	25-50		complex^T?
2080327	19:06:54	S16W83	0039	X1.0	28697	25-50		complex^T
2080602	05:18:18	N17E92	-	C2.1	108	25-50		single loop?
2081203	02:17:18	S08E86	-	C1.4	160	25-50	Y	single loop
2082336	16:10:18	S10W88	-	-	104	25-50		single loop^T
2082418	11:16:10	S05W89	0069?	-	400	25-50		complex (multi-LTs)^T?
2082803	10:59:30	S18W79	0083	C5.7	912	50-100		complex
2082809	18:10:46	N10E87	-	C6.6	784	12-25		one source (LT)
2090309	12:45:42	S08W77	0087?	C1.5	128	25-50		complex
2090608	16:27:02	S06E89	-	C9.2	752	25-50		loop not well def?
2090801	01:39:10	S11E79	0105	M1.5	1072	12-25	Y	complex
2092002	09:26:42	S25E75	0126	M1.8	1520	800-7000	Y	single loop
2111410	11:09:38	S15E71	0195?	C5.5	352	50-100		2 FPs
2112532	21:50:30	S13W89	-	C?	72	25-50		single loop
3021411	09:17:18	N12W88	-	M1.2	1072	25-50		one source
added 05/2004:								
2042101	01:30:30	S15W91	9906	X1.5	59298	800-7000	Y	complex (multi-LTs, 2-FPs)
2090708	17:41:22	S12E88	-	-	240	25-50	Y	complex (multi-LTs, 2-FPs)
3102405	02:35:34	S19E83	-	-	1587	50-100	Y	complex (multi-LTs, 2-FPs)
3110316	09:51:38	N09W77	-	X3.9	13808	300-800	Y	single loop
3110319	15:31:14	S15W72	-	-	3032	25-50	Y	complex (multi-loop, 3-FPs)
3111313	04:59:14	N02E87	0501	M1.7	1328	50-100	Y	single loop
4010604	06:25:30	N05E89	-	-	2288	800-7000	Y	complex (multi-LTs, 2-FPs)

Note — The first 22 events were selected from the period from 12-Feb-2002 through 02-May-2003; the new 7 events were from the period through 18-Apr-2004. (1) Peak counts (counts/s) are in the 12–25 keV energy band. (2) "Image spec." — Y (yes) marks a total of 11 events whose LT and FP spectra have been obtained for spectral index statistics shown in Fig. 2.10. (3) "single loop": 8 events here are of this type. (4) "complex" = complex morphology or multiple loops; 13 events fall into this category. (5) "one source" = only one source was detected; 3 events have this characteristics. (6) Out of the rest 5 events, two do not have a well-defined loop (source) structure, and the other three appear to have either LT or FP (not both) sources. (7) The superscript 'T' denotes those flares with *TRACE* data available in the *RHESSI* FOV.
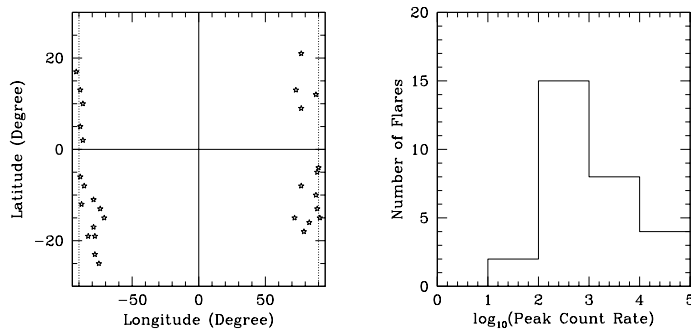

Figure 2.1: Heliographic location distribution (*left*) and histogram of the peak count rate (*right*) at 12–25 keV of the sample flares. The dotted vertical lines in the left panel marks 90° in longitude.

2.2.2 Imaging

At the time of this study, for the purpose of studying spectroscopy and light curves of individual sources using *RHESSI* data, the first step was to reconstruct images in different energy bands and/or time ranges. We describe the key points in our imaging processes below and list the details in the appendix (see § A.1).

(1) **Imaging algorithms**. Among the available *RHESSI* imaging algorithms (Hurford et al. 2002), we used Back-projection and/or CLEAN for preliminary studies, and CLEAN for light curves of individual sources as it is relatively much faster. We used much more computationally expensive PIXON for imaging spectroscopy, which is most suitable for this task because of its excellent photometry.

(2) **Integration Time Intervals.** Different time intervals were selected for different purposes. For spectroscopic images, a time interval about the peak in the 25–50 keV channel is preferred. For light curve images, we selected a time range including the rise and decay phase and divided it into a number of time bins (each bin for an image). Each time bin has an appropriate length (a multiple of the spacecraft spin period $\simeq 4$ s) to allow sufficient photon counts for imaging as well as good temporal resolution. All the time bins are selected to exclude intervals with particle events, with attenuator state changes, or with decimation state changes.

(3) **Energy Bins.** For imaging spectroscopy, the energy ranges were set as follows. The lower limit of the energy range was obtained by the attenuator states: namely, about 3 keV when none of the two attenuators is in, 6 keV when one is in, and 10 keV when both are in. The upper limit goes as high as there are sufficient signals in the images. Once the energy range was obtained we divided it into logarithmically spaced bins. Two aspects were taken into account for determining the energy bin width. On the one hand, we would like to have as many as possible bins in order to obtain a sufficiently large number of data points for spectral fits, but the smallest bin width (at the low energy end) should not be smaller than 1 keV, the nominal *RHESSI* energy resolution; on the other, we would like to have broad energy bins to increase the photon count rate in each bin for better statistical S/N in images, but it is not legitimate to construct images with an arbitrarily wide[4] energy range because the instrument response varies with energy and the imaging software only take a mean energy for computing the expected instrument response (Smith et al. 2002). For light curves, we took much broader energy bins, within which images at different energies exhibit common features.

2.2.3 Imaging Spectra and Light Curves

Once images at different energies or times are obtained, we are ready to infer spectra as well as light curves of individual sources. By examining images at various energies and times, we identified FP and/or LT sources. For each source, we selected a box to enclose it and summed over all the pixel values in this box, divided by the width of the energy bin, to get the differential photon flux. If available, images from *Transition Region And Coronal Explorer* (*TRACE*) were used to help distinguish individual sources. Plotting the

---

[4]Smith et al. (2002) recommended that the size of a energy bin should not exceeds 1/10 of its mean energy for (spatially integrated) spectroscopy. However, this requirement might be too strict imaging spectroscopy, as one usually must use relatively broad energy bins to achieve sufficient count statistics for imaging.

flux versus energy (time) results in the spectrum (light curve) and in turn the characteristics of the spectrum (light curve) provides clues on the nature of the source. For the events in which we cannot unambiguously identify the magnetic connectivity between corresponding FP and LT sources, we summed the fluxes of all the FPs.

2.3   Case Study Results

We present in this section results from selected events falling in three morphological categories: single-loop, multiple-loop, and miscellaneous types.

2.3.1   Single Loop Flares

Out of the 29 total events, eight appear to be morphologically similar to the canonical Masuda (1994) flare, namely, a LT source connected by a single flaring loop to two FPs. PIXON images of these flares were obtained around the peak time, and other times whenever the count rate was sufficiently large to allow imaging in the 25–50 keV band. We use these images as the input for imaging spectroscopy.
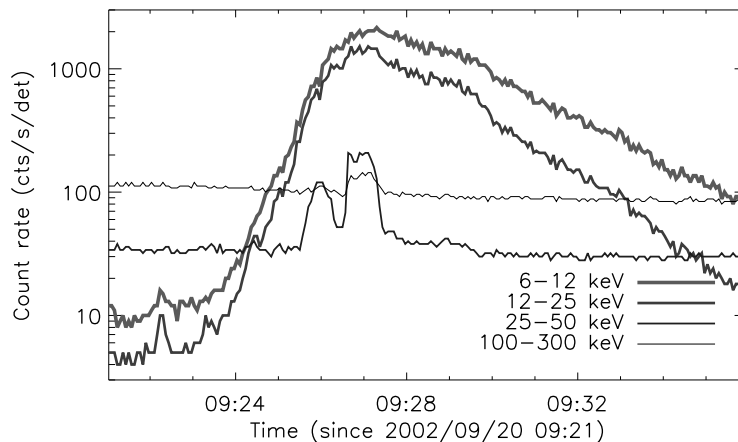
Figure 2.2: *RHESSI* light curves of the 2002 September 20 M1.8 flare (ID: 2092002).

Here we describe the 2002 September 20 flare (ID 20920020), which is a *GOES* M1.8 event observed by *RHESSI* up to 800–7000 keV. This event started at 09:22:08 UT, continued rising to a sub-peak at 09:25:59 UT in energy channel between 25 keV and 300 keV, and peaked at 09:26:42 UT nearly simultaneously in the energy channels from 6 keV through 300 keV as can be seen from the light curves in Figure 2.2. We focus on the impulsive phase here. The decay phase of this flare was studied by Jiang et al. (2006).

The HXR images were reconstructed by the PIXON algorithm using front segments of detectors 3 through 6, and detectors 8 and 9, with a minimal spatial resolution of 7″. Figure 2.3 shows the resulting images in separate energy bands for a time interval [09:26:36, 09:27:20 UT], covering the main peak. It is clearly shown that in the 11.1–12.4 keV image a diffuse source dominates, suggesting a hot LT source. Two FP sources appear in about
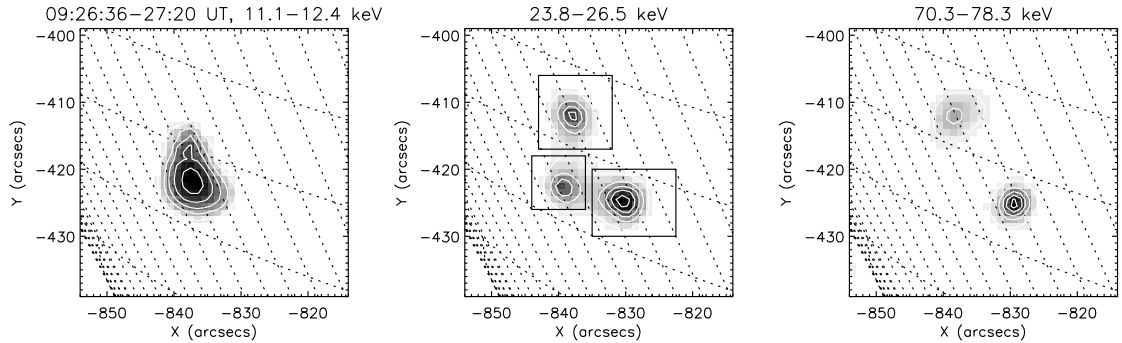
Figure 2.3: Hard X-ray images of flare 2092002 at different energies. The white contours are at the 10%, 30%, 50%, 70%, and 90% levels of the maximum of each panel. We show in the middle panel three boxes defined to enclose individual sources to infer their spectra and light curves.

23.8–26.5 keV and become more and more dominant at higher energies. Note the southern FP is much brighter than the northern one, which may be due to possible asymmetric convergence of the magnetic loop. That is, the loop may converge more rapidly approaching to the northern FP and this result in a stronger magnetic mirroring effect which suppresses the number of high-energy electrons that reach the chromosphere there. We will address asymmetric FP emission in depth later (see Chapter 5).
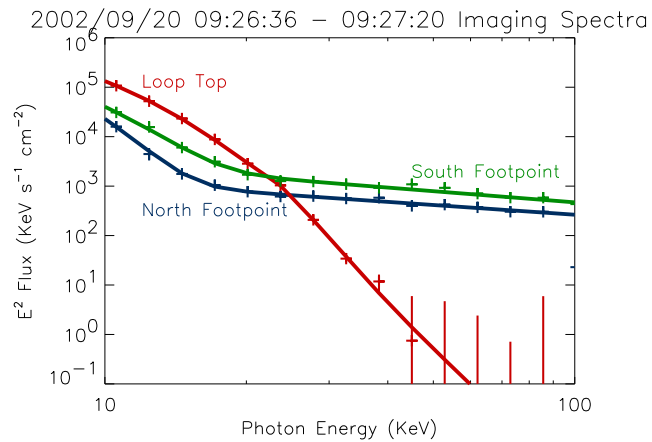
Figure 2.4: νf_ν spectra of the LT and FP sources of flare 2092002. The thick lines are fits from a thermal plus power-law model [from Jiang et al. 2003].

We used the boxes shown in Figure 2.3 (*middle*) to define the three sources and integrated the photon flux within each box to obtain the corresponding spectrum, which is shown in Figure 2.4. We (Jiang, Liu, Petrosian, & McTiernan, 2003) then fitted each spectrum with a thermal plus power-law model. The best fit suggests the LT source (fitted within 10–57 keV) has a temperature $k_{\mathrm{B}}T = 2.22\,\mathrm{keV}$. The two FPs have a weaker thermal component ($k_{\mathrm{B}}T = 1.31, 1.82\,\mathrm{keV}$) and a stronger power-law component, with an index of $\gamma = 2.65, 2.75$ for the northern and southern one, respectively.
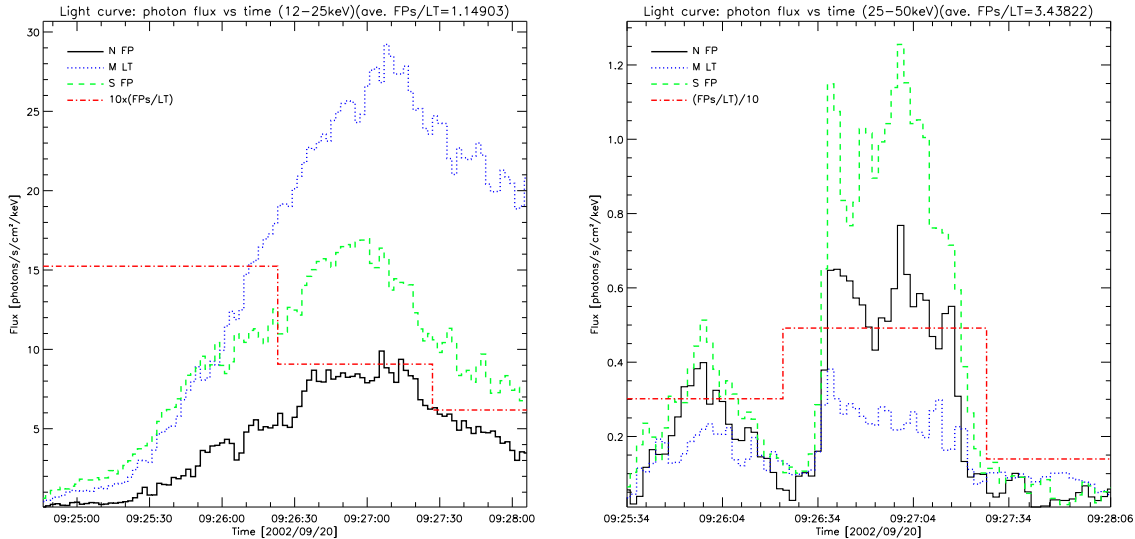
Figure 2.5: Light curves of individual FP and LT sources in the 12–25 keV (*left*) and 25–50 keV (*right*) energy band for flare 2092002. The dot-dashed, step-shaped curves show the ratio of flux of the two FPs to the LT sources, averaged over time intervals before, during, and after the peak. "N FP" refers to the northern FP, "M LT" the middle LT, "S FP" the southern FP.

We also used the boxes defined in Figure 2.2 to infer the light curves of individual sources. Figure 2.5 shows such light curves at a cadence of 2 s with about a 4 s integration time in the 12–25 keV and 25–50 keV band. The ratio of the fluxes of the two FPs combined to the LT source averaged over the rise, peak, and decay phase, respectively, is shown as the dot-dashed line. We note that the LT source dominates at 12–25 keV and its importance gradually increases with time; in contrast, the FP sources are much brighter in the 25–50 keV channel but it decreases more rapidly after the peak. We note that from the first pulse to the second (as seen at 25–50 keV), the LT emission is essentially constant at 25–50 keV band but increases substantially in the 12–25 keV band. This suggests the LP spectrum undergoes softening.

2.3.2   Multiple Loop Flares

In the selected sample, 13 flares appear to have a more complex morphology, one[5] of which was identified as a multiple-loop event, similar to those studied by Petrosian et al. (2002) during the rising phase of solar cycle 23. This event (ID: 2080327), is an X1.0 flare, occurring in AR10039 on 2002 August 03. Figure 2.6 shows the light curves (*left*), which exhibit a complex history, with multiple pulses appearing at high energies ($\gtrsim$50 keV).

Figure 2.7 shows *RHESSI* image contours at different energies superimposed on a *TRACE* 171 Å image. As is evident, the HXR source morphology is more complex than the 2092002 flare. At high energies, there are several sources (presumably FPs) located inside the limb. At low energies, the structure appears simple, with a single source (LT) appearing above

---

[5]The other complex events require further analysis of light curves and imaging spectroscopy, as well as multiple-wavelength observation to distinguish individual sources.
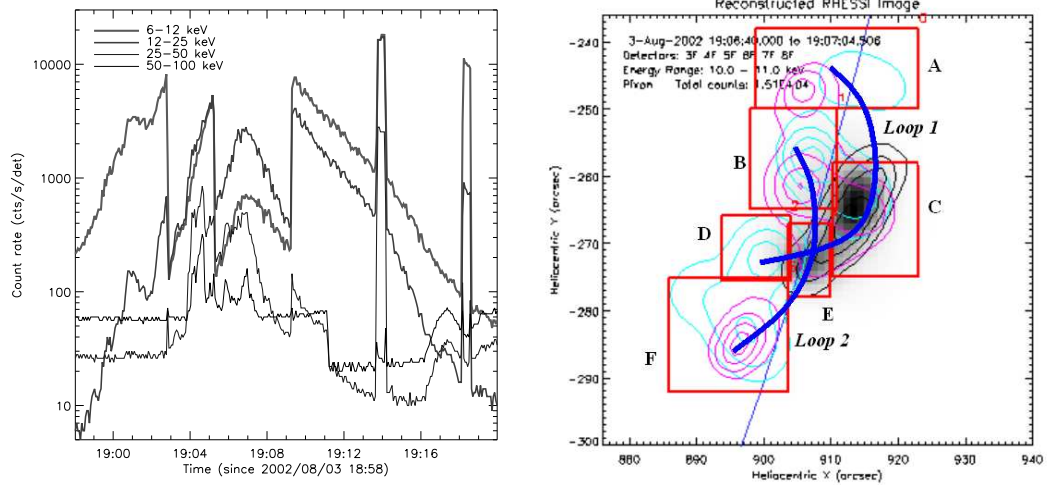
Figure 2.6: Light curves (*left*) and PIXON images, together with boxes enclosing individual sources (*right*), of the 2002 August 03 X1.0 flare (ID: 2080327). The artificial jumps of the count rates (*left*) are due to the changes of the attenuator state. The background map and the contours are images at different energies, same as those shown in Fig. 2.7. Two major flaring loops, marked with thick curves, are identified, and their corresponding LT and FP sources are assigned a letter, A, B, C, etc.

the limb. However, its elongate shape and the existence of many FP sources suggest that this simple appearance could be a projection effect and there are probably more than one LT sources (but not resolved by *RHESSI*). The *TRACE* image was recorded at a later time (19:32:37 UT) during the flare and was selected in order to show the coronal loop structure in EUV, which reveals an arcade of a series of magnetic loops. Two of these loops seem to be cospatial with the *RHESSI* sources, and based on this, we group the HXR sources in two loops, as shown in Figure 2.6 (*right*). Sources A, C, and D are of loop 1, and the others are of loop 2.

Again we obtained the light curves (Fig. 2.8) of the individual sources by integrating fluxes in the boxes (see Fig. 2.6, *right*). We note that the two loops do not contribute equally to the total emission. In the 25–50 keV band, the total flux of loop 2 is higher during the first pulse but lower in the second than that of loop 1; in the 12–25 keV channel, the LT source of loop 2 is stronger than that of loop 1 by a factor of ~2 during the first pulse (although their total fluxes are comparable at this time), but much weaker by a factor of 4 in the second pulse (and the total flux of loop 2 is lower too). The LT emission from loop 1 dominates over others in the second (major) peak in both energy channels. In the 25–50 keV band, the total flux of loop 1 (2) increases (decrease) from the first peak to the second. This suggests that the burst of loop 1 may be initiated by its interaction with loop 2.

2.3.3 Miscellaneous Types

In six events of this sample, not both LT and FP sources are present. Based on their locations, light curves, and spectra, out of these six flares, we find that three appear to have only a LT source, one seems to have *two* LT sources (beyond the limb), and the other two seem to have only FP sources (see Table 2.1).
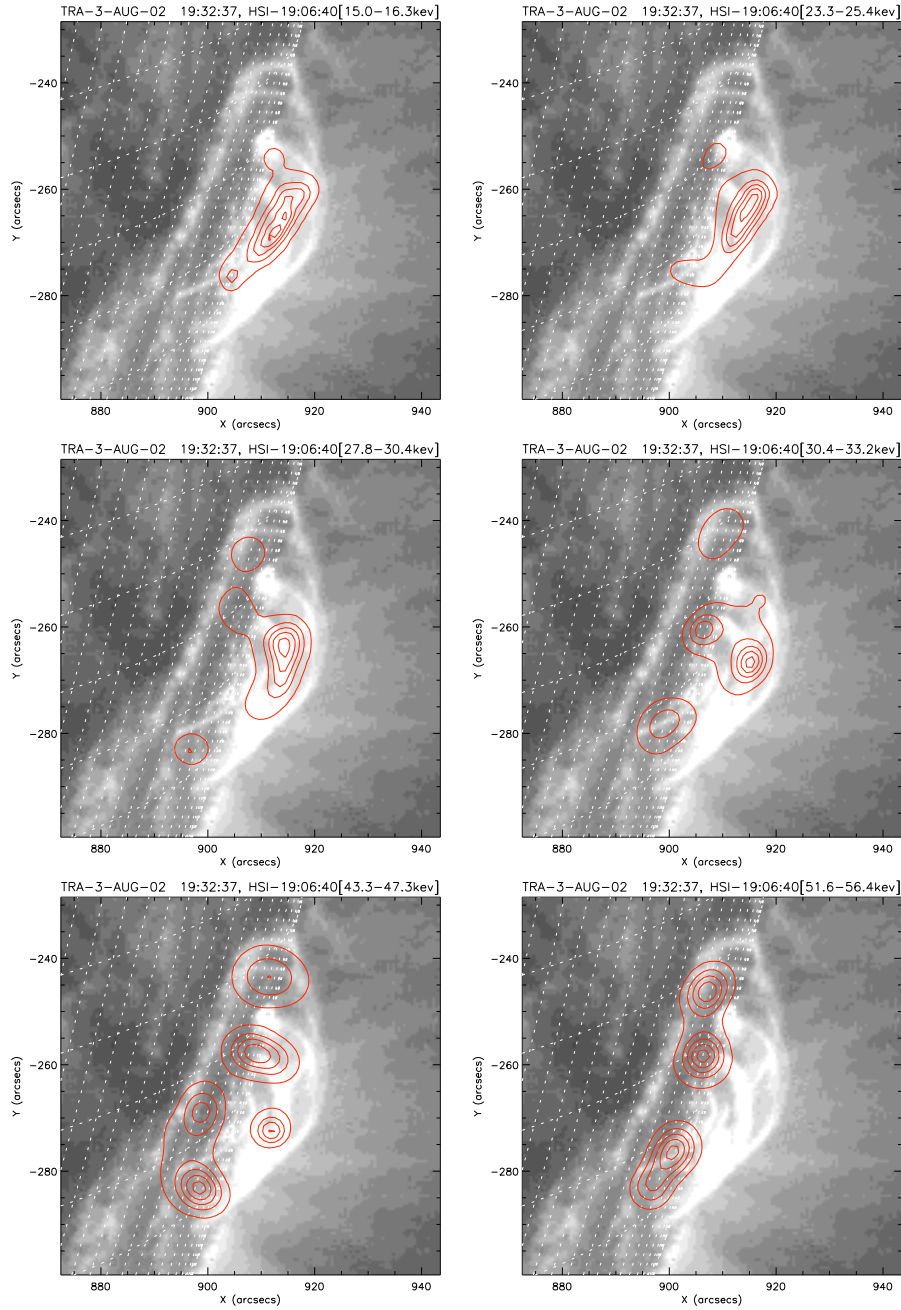
Figure 2.7: *RHESSI* HXR contours at different energies superimposed on a *TRACE* 171 Å images for flare 2080327. Heliographic grids (*dotted lines*) have a 1° spacing in both longitude and latitude.
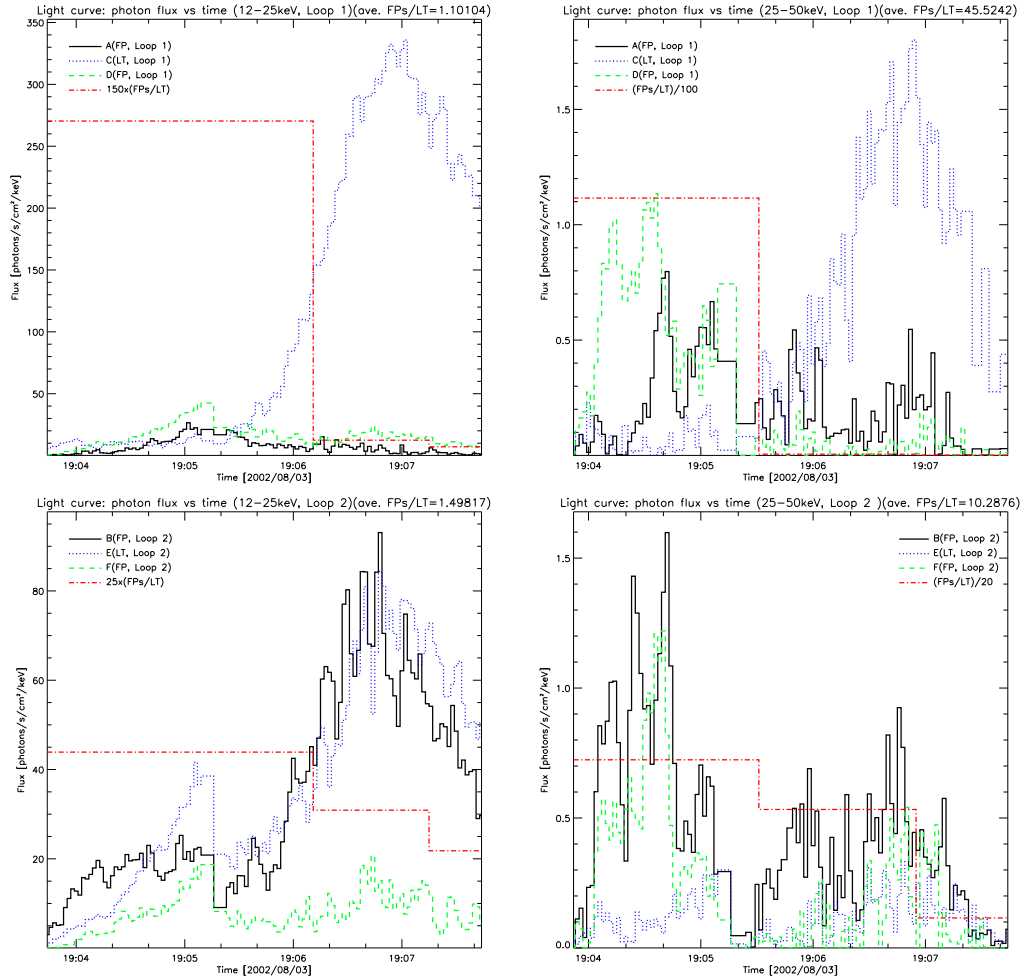
Figure 2.8: Same as Fig. 2.5, but for the two loops of flare 2080327. The upper panels are for loop 1 (see Fig. 2.6, *right*) in 12–25 keV (*left*) and 25–50 keV (*right*); the lower panels are for loop 2.

Flare 2082809 (C6.6), occurring on 2002 August 28, is a single LT source flare, without FPs detected. In the PIXON images at around the peak time, this event appears as a single source on the limb (see Fig. 2.9, *left*) in all the 13 energy bins from 10 to 54.2 keV. CLEAN images at different times also indicate a single source. Fits to the spatially integrated spectrum yield a power law index of 5.0 (steep) and a temperature of 1.9 keV, suggesting this source is a LT, presumably with its corresponding FPs being occulted behind the limb.

Flare 2111410 (2002 November 14, C5.5), does not show an appreciable LT source possibly because the LT is too faint to be detected (i.e., out the *RHESSI* dynamic range) and/or the angular separation is not sufficient between the LP and FPs, considering its low heliocentric longitude of 71°, the lowest in this sample of the 29 flares.
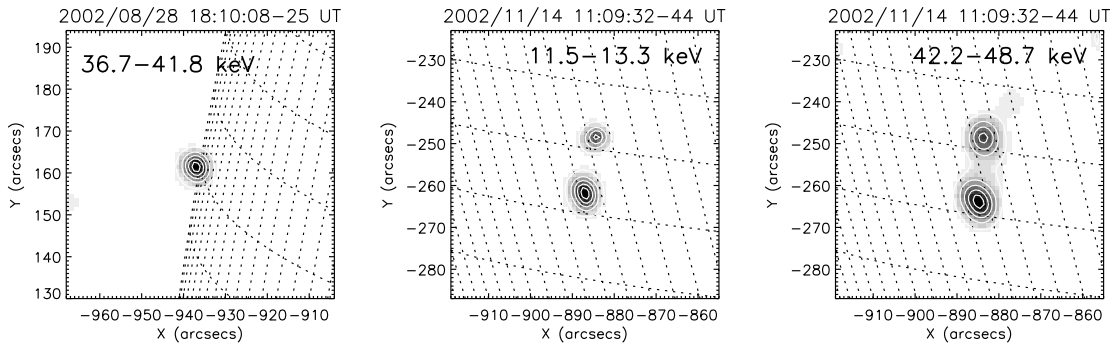
Figure 2.9: Images of flare 2082809 at 36.7–41.8 keV (*left*) and flare 2111410 at 11.5–13.3 (*middle*) and 42.2–48.7 keV (*right*).

2.4 Statistical Results

2.4.1 Imaging Spectroscopy

Figure 2.10 (*left*) shows the histogram of LT and FP spectral indices from single power-law fits for a set of 11 limb flares (i.e., those marked with "Y" in the "Image spec." column of Table 2.1). Several flares with multiple pulses have multiple entries in the data set. In general, the LT spectra are steeper than those of the FPs. The means of the two distributions are $\bar{\gamma}_{\text{LT}} = 6.84$ and $\bar{\gamma}_{\text{FP}} = 3.35$ and yield a large difference of $\Delta\bar{\gamma} = 3.49$, which could be expected from the stochastic acceleration model (Petrosian & Liu 2004). Such a large difference is also seen for some of the individual flares as shown in the scatter
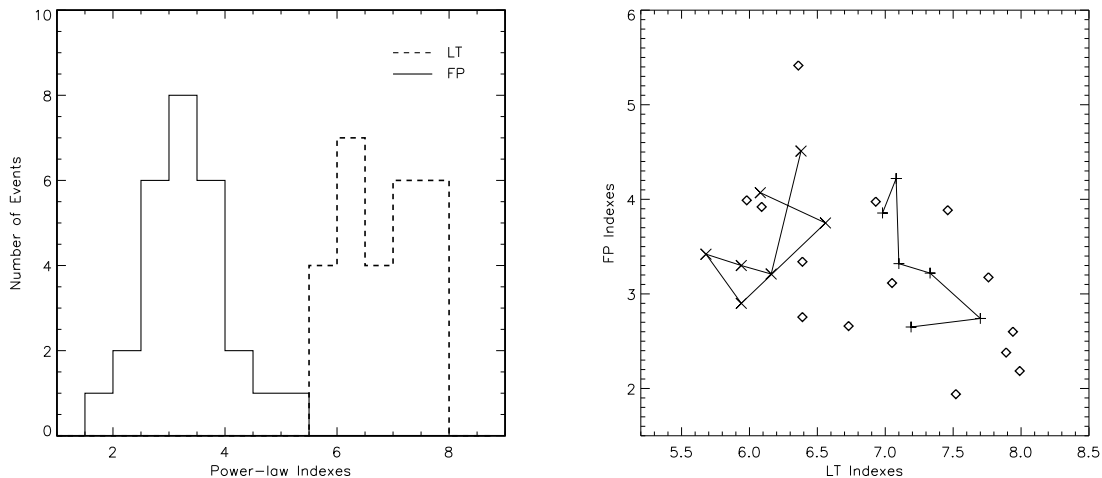

Figure 2.10: *Left*: Histogram of LT and FP spectral indices during the impulsive peak for a sample of 11 limb flares (see Table 2.1). *Right*: The spectral indices of the LT vs FP sources for the same sample. The data set also includes the first (*cross*) and second (*plus*) pulses of the 2003 November 03 flare (see Chapter 3), for which the data points are connected by lines.

plot on the right panel for the same flares. Note that Petrosian et al. (2002) obtained $\bar{\gamma}_{LT} = 6.2 \pm 1.5$ and $\bar{\gamma}_{FP} = 4.9 \pm 1.5$ from broadband *Yohkoh* data. The main difference between our and their results is that our FP spectra are harder, which can be ascribed to the different flare sample selected here and/or the higher energy and spatial resolution *RHESSI* has as compared with *Yohkoh*.

However, one would also expect some correlation between these indexes which does not seem to be present. In this figure we also show the evolution of these indexes for the 2003 November 03 X3.9 flare (see Chapter 3), whenever both the LT and FP sources can be fitted with a power law model. During the first pulse (cross signs) the spectral indexes seem to be correlated weakly, but not during the second pulse (plus signs), which appears to be still in its rising phase (see Fig. 3.3) and a weak anti-correlation is seen in the index values. The correlation expected from the simple model is clearly not present. But this is not surprising. Firstly, the actual LT and FP spectra and expressions for loss and escape
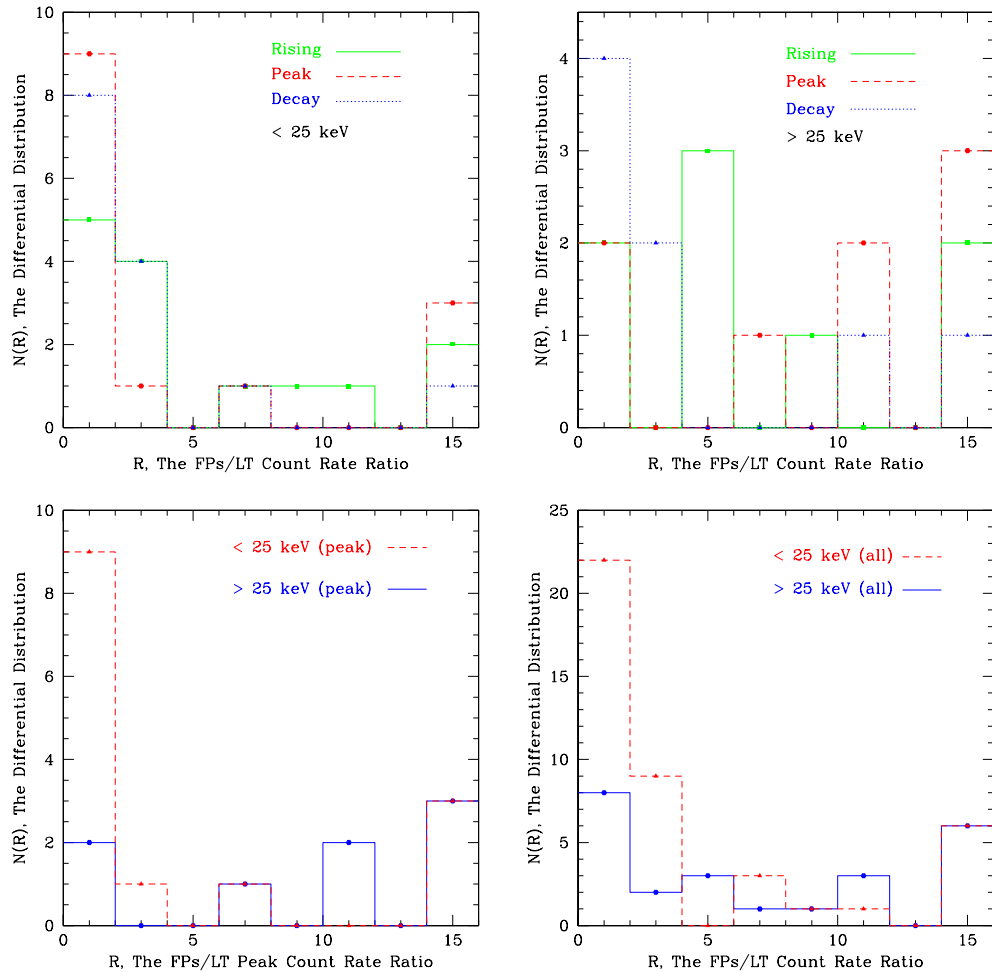

Figure 2.11: Histograms of R, the FPs to LP flux ratios at different times and energies, with a bin size of 2. The upper cutoff is set at 16, about the upper limit of *RHESSI* images, and any ratio greater than this value is counted to the last bin (note this results in the tail bump at $R = 16$).

times are more complicated (see Chapter 7). Secondly, the observed LT indexes are more representative of the spectrum at lower energy (where the spectrum is steeper) than those of the FPs. These indicate that we need to carry out more accurate data analysis and use more accurate models than the toy model given earlier.

2.4.2   Statistics of the Relative Fluxes: FPs vs. LTs

For ten of the sample flares, we have obtained the light curves of individual LT and FP sources and their flux ratios. Histograms of the FP-to-LT flux ratio are shown in Figure 2.11, which reveals the following characteristics.

1. Again, we find that the LT sources have softer spectra than the FP sources (see the *lower right* panel). At low energies (≤ 25 keV), the median of flux ratio distribution is very close to one; in contrast, at high energies (≥ 25 keV), the median ratio is much greater than unity and its distribution is much flatter. These results are qualitatively consistent with the theoretical calculations by Petrosian and Liu (2004).

2. At flare peak times, the LT emission dominates at low energies (with the ratio distribution concentrated close to unity) while FPs dominate at high energies (*lower left* panel).

3. During the decay phase of a flare (*upper* panels), the LT source tends to be the major contributor to the total flare emission, especially at low energies (≤ 25 keV).

4. At high energies (≥ 25 keV), the median of the distribution first increases (from the rise to the peak phase) and then decreases, which translates to that the relative importance of the FP emission has an up-and-down variation. This LT-FP-LT pattern is correlated with the commonly observed soft-hard-soft variation in the spatially integrated spectrum during the course of a flare, and this suggests such a spectrum variation is (at least partly) contributed by the transition between the spatial variation of the dominant emission.

2.5   Flare Statistics and Selection Biases

The study described above is appropriate for a small sample of flares. To uncover the general characteristics of flares, it is necessary to have statistical studies of the parameters (e.g. peak X-ray flux and duration) for a much larger number of flares. Here we briefly describe the background of this subject and propose an approach for a future study.

   Several statistical investigations of distributions, ranges and mean values of relevant parameters, and the correlations between them have been carried out (see, e.g., Lee et al., 1993, 1995; Petrosian et al., 2002) using statistical methods developed by Efron & Petrosian (1992, 1995). Similar statistical studies were done by many others as well (e.g., Dennis, 1985; Crosby, Aschwanden, & Dennis, 1993; Dennis & Zarro, 1993).

   One of the most important aspects of this kind of study is proper accounting of the selection biases. The first step here is the careful selection of the sample. The left panel of Figure 2.12 shows a representative distribution of peak count rates of *RHESSI* flares.
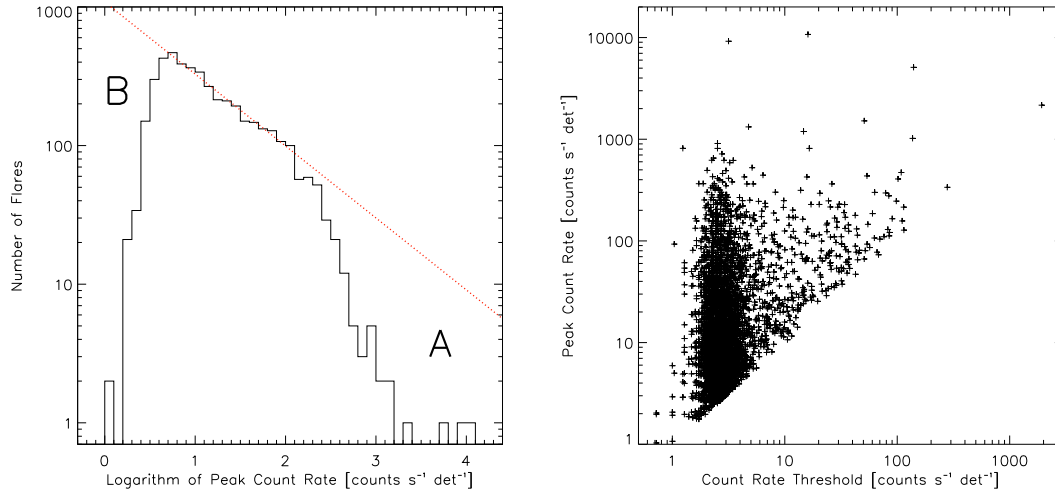
Figure 2.12: *Left*: Distribution of the *RHESSI* flares with peak count rates (in the 12–25 keV channel) greater than 4σ above the background noise and when no shutters were in, the latter of which introduces the bias at high count rates in region A that can be corrected. The bias at low count rates (region B) is due to variation of the detection threshold as shown on the *Right*, which shows the peak count rate vs. the threshold count rate for these flares. The truncation of the data below the diagonal line is obvious.

It clearly suffers from bias at high peak count rates (A) from the effects of the *RHESSI* shutters and at low peak rates (B) due to background variations. A flare usually is identified when its count rate in some channel is more than several sigmas above the background noise. This means that the threshold for detection varies from flare to flare and with the energy band due to different background. The right panel of Figure 2.12 shows the peak count rate versus the threshold count rate of the flares used in the left hand side plot. It is clear that the sample is biased against identification of weaker flares, as shown by the truncation of the data below the diagonal line, when the background level, and hence the count-rate threshold, is higher. Less obvious but no less real is the truncation above a peak rate of about 100 counts s^{-1}detector^{-1} due to the insertion of the *RHESSI* shutters for these more intense flares. This kind of biased or truncated data can be analyzed using our statistical methods (Efron & Petrosian 1992, 1999). Several other characteristics of flare emission, e.g. duration and spectrum, also influence the sample selection process (see Lee et al. 1993, 1995), and will require similar thorough statistical treatment.

Su, Gan, & Li (2006) have recently reported a statistical study on *RHESSI* peak count rates and various (rise, decay, and duration) timescales, using data in the 12–25 keV band which was taken directly from the online flare list without proper corrections. For example, they used a simple, empirical method to account for the different attenuator states. They found a power-law index of 1.80 ± 0.02 for the peak count rates, but this may be subject to improper consideration of the instrument response and selection biases mentioned above.

In the near future, as the *RHESSI* calibration and software are improved and become more stable, we plan to carry out a similar analysis for more flares, carefully correcting various biases. The peak X-ray flux would be the first parameter to be studied. For each

flare in the *RHESSI* flare list, one should use the detector response matrix (DRM) to convert the count rate to the incident photon rate and properly subtract the background, using the *RHESSI* spectral analysis software package, Object Spectral Executive (OSPEX).. An automated tool will be developed to perform this analysis. The statistical methods quoted above will be used to correct selection biases. Similar analysis will be applied to other flare parameters, e.g. duration and total counts.

We expect to obtain the intrinsic distribution of these flare parameters and their correlation with much higher accuracy and sensitivity benefiting from the superior capabilities of *RHESSI*, and compare the results with those from earlier missions. This will provide important implications to flare energization and particle acceleration. Examples of such implications include addressing the question that whether numerous small flares play a significant role in coronal heating (Lee et al. 1993).

2.6 Summary and Discussion

We have initiated an investigation of a sample of *limb flares* observed by *RHESSI*. We used X-ray images to infer flaring loop structures and to distinguish between FP and LT sources. We analyzed the light curves and spectra of these individual sources, and presented the statistics of the spectrum indexes, as well as the FP-to-LT flux ratio during different phases of a flare. The preliminary results from a sample of 29 flares are as follows.

1. The averages of the LT and FP spectral indexes are 6.84 and 3.35, respectively, with a large difference of 3.49, which can, in principle, be used to constrain the parameters in the particle acceleration model.

2. An expected correlation between the LT and FP spectral indexes is not present in this study, suggesting that a more accurate statistical study (with a larger sample) is required and a more rigorous prediction from the particle acceleration model is needed as well.

3. At flare peak times, the LT (FP) emission dominates at low (high) energies. During the decay phase, the LT emission becomes more important than the FP emission. The LT-FP-LT variation of relative importance of HXR emission is correlated with the soft-hard-soft variation of the spatially integrated spectrum.

We have also proposed a plan for future statistical studies (in addition to expanding the sample of flares for imaging spectroscopy analysis), in which using proper statistical methods to correct data selection biases is required to uncover the intrinsic distribution of various flare parameters.

The statistical study presented here, in practice, also served as data mining to identify several interesting flares for detailed investigations. Studies of these particular events will be presented in next four chapters.